IOP Publishing

Nanoscale Energy Transport
Emerging phenomena, methods and applications
Bolin Liao

Chapter 9

Ultrafast thermal and magnetic characterization of materials enabled by the time-resolved magneto-optical Kerr effect

Dustin M Lattery, Jie Zhu, Dingbin Huang and Xiaojia Wang

As traditional complementary metal oxide semiconductors struggle to extend previous industrial trends, new technologies must be researched and delivered. One of the most important aspects that must be considered is the transport of heat within the material. By advancing the design of materials and interfaces, heat transfer within electronic devices can be improved. At the same time, novel technologies that rely on the magnetism of thin films also need to have their transient magnetic behavior optimized. By measuring the magnetic response of the materials, engineers can select the best-matched materials to design and fabricate devices with lower power consumption and higher processing speed and thus improved performance. Such material transport studies require new methods and metrology development that can provide highly sensitive and accurate characterization of the materials. The time-resolved magneto-optical Kerr effect (TR-MOKE) technique is capable of probing both the thermophysical and magnetic properties of a variety of materials, and it offers superb spatial (micrometer) and temporal (sub-picosecond) resolutions. In this chapter, we provide information about this technique through examples of its application in the study of thermal transport and magnetization dynamics. We then highlight several novel research directions that are potentially enabled by this technique, thus expanding the applications of TR-MOKE to form a more comprehensive picture of energy transport.

doi:10.1088/978-0-7503-1738-2ch9

9.1 Introduction

9.1.1 Background and motivation

Transport properties (e.g. electrical conductivity, thermal conductivity and the transfer of magnetic moment of materials) are of critical importance in a broad range of engineering applications. In this chapter, we highlight the state-of-the-art time-resolved magneto-optical Kerr effect (TR-MOKE) methodology, based on the ultrafast pump–probe technique, for characterizing the thermal and magnetic transport properties of several representative materials. These materials are of technological importance, serving as building blocks for the next generation of electronic, spintronic and data storage devices. For decades, these device components have been manufactured following Moore's law which states that the number of transistors per chip should double every two years [1]. Semiconductor industries have pushed to maintain this trend, but they are finally being limited by the power density of device operation, or more simply, heat extraction [2]. By moving electrons through more closely spaced transistors at faster switching speeds, these devices are producing progressively more dense heat loads, imposing a continually growing need for thermal management (the capability of redistributing and removing heat). The solutions proposed by researchers have followed two main paths: (i) developing new technologies that require less power and (ii) engineering new materials and better interfaces that can be scaled down without increasing heat generation or impeding heat transfer.

Following the first path, the field of spintronics (spin-electronics) has proven a promising direction since the discovery of giant magnetoresistance [3, 4]. On the fundamental level, spintronics focuses on advancing materials by manipulating the magnetization (or spin) in magnetic materials to achieve so-called 'beyond CMOS' (complementary metal oxide semiconductor) technologies. Theoretically, spintronic devices have the benefits of minuscule amounts of power being required for switching, fast switching speeds and non-volatility (i.e. they do not require power to retain information), making them ideal for both processing and memory. Spintronics have already been adopted in widespread applications. The most common application can be found in magnetic random-access memory (MRAM), which has rapidly gone from utilizing the magnetic field to switch memory [5], to spin-transfer torque-MRAM [6, 7] and to spin-orbit torque-MRAM [8, 9], making use of cutting-edge physics along the way. The unique advantages of these memory technologies have further enabled advanced applications in all-spin logic (using only spin transport for computation) [10, 11], probabilistic computing [12], spin torque oscillators [13–16] and heat-assisted magnetic recording (HAMR) [17–19], among others. For these technologies, it is crucial to understand the magnetic properties (such as the Gilbert damping α) of materials at short time scales (e.g. sub-nanosecond) to guide further research and development.

The characterization of magnetic material properties has often exploited the technique of ferromagnetic resonance (FMR) [20]. Generally, FMR uses a microwave signal to excite a magnetic sample. The change in magnetic susceptibility of the sample is measured as the sample goes through its resonance condition, during

which the external field and frequency agree with the Kittel dispersion for resonance [21]. The resulting microwave absorption, as a function of frequency or field, can be fitted to a Lorentzian or anti-Lorentzian function, where the width of the Lorentzian (the so-called linewidth) is dependent on the damping parameter α [22]. While this highly versatile technique has adapted advancements (such as stripline FMR and others [23]), it has difficulty characterizing new technologically relevant materials with large perpendicular magnetic anisotropy (PMA). The large anisotropy requires a high-power input to excite the magnetization, and the relatively large damping of metallic materials intrinsically leads to large linewidths. The search for alternative measurement techniques has been motivated by these challenges faced by FMR.

Along the second path of material engineering solutions, electronics research has continued in the categories of materials innovation and heat dissipation (particularly in high-flux and high-voltage power electronics). Recent developments in materials and in device miniaturization have created new opportunities but have also imposed challenges for the science of thermal transport and the technology of thermal management [24]. Advances in synthesis, processing and microanalysis are enabling the production of well-characterized materials with structural features ranging in size from micrometers down to nanometers. Enormous attention has been paid to functionalized structures such as superlattices, multilayer coatings, nanowire arrays and polymer nanocomposite materials [25–31]. Thermal interface materials and thermal fluids have drawn growing attention in both industry and the military for cooling of electronics [32–34]. Emerging two-dimensional (2D) materials such as graphene, hexagonal boron nitride (h-BN), black phosphorus (BP) and MoS_2, as well as bulk β-Ga_2O_3, have been considered as building blocks for future electronics [35–38]. Their anisotropic thermal transport properties, induced by the materials' structures, need to be understood more comprehensively to advance device performance.

9.1.2 Ultrafast-laser-based metrology for transport studies

For these emerging materials and technologies, ultrafast laser-based pump–probe techniques provide sensitive, powerful and high-throughput capabilities for the study of transport in materials. The high-temporal resolution of the ultrafast pump–probe method makes it suitable for studying dynamics occurring on time scales from hundreds of femtoseconds (fs, 10^{-15} s) to several nanoseconds (ns, 10^{-9} s), for both thermal and magnetic transport processes. The basic pump–probe configuration is time-domain thermoreflectance (TDTR) [39–41], which detects the temperature-dependent reflectance of the sample to extract the materials' thermal properties [41–53] or to quantify thermal transport across interfaces [54–58]. When integrated with the 'beam-offset' approach, TDTR can probe thermal transport, along both the through-plane and in-plane directions, to reconstruct the three-dimensional (3D) thermal conductivity tensor of thermally anisotropic materials [59, 60]. This method has been successfully demonstrated for certain materials [59–62]; however, it has also been proven to produce low measurement sensitivity to the in-plane thermal transport in materials with low thermal conductivity [63]. This is mainly attributed

to the significant lateral heat spreading in the transducer layer during TDTR measurements, which smears out the thermal information of the underlying sample. Therefore, the transducer layer for TDTR measurements is preferred to have a low thermal conductivity to improve the measurement sensitivity to the in-plane thermal transport properties of the sample materials.

The TR-MOKE, a system initially invented to probe magnetization dynamics [64, 65], can be extended to thermal measurements by taking advantage of the temperature-dependent magnetization of the transducer. Therefore, TR-MOKE can be essentially treated as an upgraded version of a standard TDTR system [63, 66]. TR-MOKE uses optically thin magnetic transducers that are immune to contamination by thermoreflectance signals from the sample beneath and thus provides greatly enhanced measurement sensitivity to in-plane thermal transport. For magnetic transport studies, TR-MOKE can detect magnetization dynamics of materials with superb spatial (diffraction-limited beam spots) and temporal (sub-picosecond) resolutions. Particularly, the use of optical pumping and detection in TR-MOKE allows it to capture the ultrafast magnetization of 'hard' materials (with large magnetic anisotropy) that are not detectable using conventional FMR methods.

In this way, TR-MOKE provides a unique capability of studying the transport properties (both thermal and magnetic) of engineered materials, and it can enable exciting new technologies. Within this chapter, we aim to provide the foundation of the TR-MOKE technique, detail the information about data reduction for magnetization dynamics and thermal transport, and discuss several representative applications enabled by this promising technique.

9.2 TR-MOKE measurement technique

MOKE allows for direct optical measurements of the magnetic state of a material. To reveal the correlation between the optical response and the magnetism of the material, this section will discuss the physical foundation of MOKE measurements, the relationship between TR-MOKE signals and the thermal and magnetic transport properties of thin-film samples, and the typical optical set-up of TR-MOKE in the pump–probe configuration.

9.2.1 The physical foundation

As first described by Kerr [67], MOKE is a process that alters the polarization state of light reflected by a magnetic material. Fundamentally, MOKE stems from the different interactions of left- and right-circularly polarized light within a magnetized material. Linearly polarized light can be represented as the sum of equal proportions of left- and right-circularly polarized light, and each type of circular polarization will experience a different phase shift and absorption when interacting with a magnetic material [68]. The result of this process is the transformation from a linear polarization to an elliptical polarization upon the reflection of light (or transmission of light, for the analogous Faraday effect), as shown by figure 9.1.

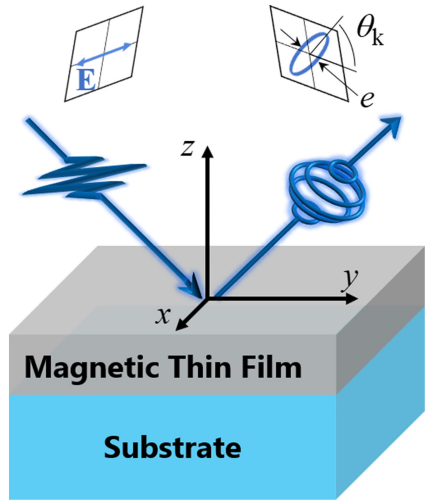

Figure 9.1. An illustration of the complex polarization rotation of reflected light from a magnetic material known as MOKE. The rotation of the polarization, from a linear polarization to an elliptical polarization, is denoted by the Kerr angle (θ_k). The ellipticity is denoted by e.

The rotation of linearly polarized light can be described by the response of an electric field vector to the dielectric tensor $\bar{\varepsilon}$, which is given by

$$\bar{\varepsilon} = \begin{pmatrix} \varepsilon_{xx} & \varepsilon_{xy} & \varepsilon_{xz} \\ -\varepsilon_{xy} & \varepsilon_{yy} & \varepsilon_{yz} \\ -\varepsilon_{xz} & -\varepsilon_{yz} & \varepsilon_{zz} \end{pmatrix}. \tag{9.1}$$

For an isotropic, non-magnetic material, the diagonal components of this tensor are equal ($\varepsilon_{xx} = \varepsilon_{yy} = \varepsilon_{zz}$), and the off-diagonal components are 0. For isotropic magnetic materials, however, the off-diagonal terms are related to the magnetization vector ($\mathbf{M}$) through

$$\bar{\varepsilon} = \varepsilon_{xx} \begin{pmatrix} 1 & -\mathrm{i}Qm_z & Qm_y \\ \mathrm{i}Qm_z & 1 & -\mathrm{i}Qm_x \\ -\mathrm{i}Qm_y & \mathrm{i}Qm_x & 1 \end{pmatrix}, \tag{9.2}$$

where Q is the magneto-optical constant and $m_i = M_i/\|\mathbf{M}\|$ [69–72]. These nonzero off-diagonal terms cause different polarization changes to the opposing circular polarizations. This leads to a complex rotation angle of the polarization, given by $\tilde{\theta} = \theta_k + \mathrm{i}e$, where the real part of $\tilde{\theta}$ is the Kerr rotation and the imaginary part is the ellipticity [70, 71]. $\tilde{\theta}$ is also sometimes presented as components of a complex permittivity tensor [73]. Our discussion in this chapter will be limited to a discussion of the real component of the Kerr rotation, θ_k, the real rotation of the major axis of polarization upon reflection of linearly polarized light.

At equilibrium, θ_k contains information about the magnetization state in magnetic materials. It is therefore adopted as an alternative method for measuring

magnetic hysteresis loops [74], in addition to vibrating sample magnetometry, alternating gradient magnetometry, and superconducting quantum interference device measurements. The MOKE response has proven to be powerful for measuring the magnetic properties of nanomaterials, including ferromagnetic monolayers [75]. MOKE microscopy has also been utilized to sense domains in magnetic materials, owing to the large contrast resulting from the opposite Kerr rotation of antiparallel magnetization between domains [76, 77]. These optical studies demonstrate well the use of MOKE for investigating magnetostatics (i.e. the magnetization of the sample is not changing in time). In the following sections, we will focus on transient magnetization dynamics induced by ultrafast laser pulses.

9.2.1.1 Ultrafast demagnetization induced by laser heating

The application of time-resolved Kerr rotations for ultrafast metrology began as a method to determine the non-equilibrium processes initiated by ultrafast laser excitation in ferromagnetic nickel [78]. Through MOKE, the magnetization within the sample can be measured, providing a window into the temperatures of various energy carriers, including electrons, phonons and magnons (wave-like variations in the magnetization). Due to the limitation of using lasers with pulse durations on the order of tens of picoseconds, early TR-MOKE measurements of ferromagnetic materials were unable to directly show these temperatures of carrier populations out of equilibrium with each other (the non-equilibrium regime) [79]. With the new application of femtosecond laser pulses (~60 fs), Beaurepaire *et al* were able to capture a sub-picosecond reduction in magnetization (demagnetization) resulting from the laser induced heating [80]. After several picoseconds to tens of picoseconds following laser excitation, the energy carriers approach thermal equilibrium, and the energy transfer will then be dominated by thermal transport via heat conduction. The temperature decay in the sample system can then be described by heat diffusion, which depends on the thermal conductivity (Λ), volumetric heat capacity (C) and the interfacial conductance (G) of the multi-layers and interfaces within the sample. The discussion of extracting these thermal parameters from the TR-MOKE signal is detailed in section 9.3.

9.2.1.2 Precessional magnetization dynamics

In addition to thermal information, this ultrafast demagnetization from laser pulses also initiates magnetization dynamics governed by the Landau–Lifshitz–Gilbert (LLG) equation, specifically magnetization (spin) precession [81, 82]. Further research into this all-optical, pump–probe technique showed that the frequency of magnetic precession extracted from TR-MOKE is consistent with frequency-domain FMR results [64]. The working principle for spin precession measured with TR-MOKE consists generally of three distinct regions, as illustrated in figure 9.2 [40, 64]. Initially, the magnetization $\mathbf{M}$ is in equilibrium and is parallel to the effective field ($\mathbf{H}_{\text{eff}} = -\nabla_{\mathbf{M}} F$, with F being the magnetic free energy density), which is the minimum energy direction for the magnetization. Then, the pump beam deposits energy into the magnetic material, heating it up and inducing thermal demagnetization. Because of the heating, both the material's saturation magnetization (M_s)

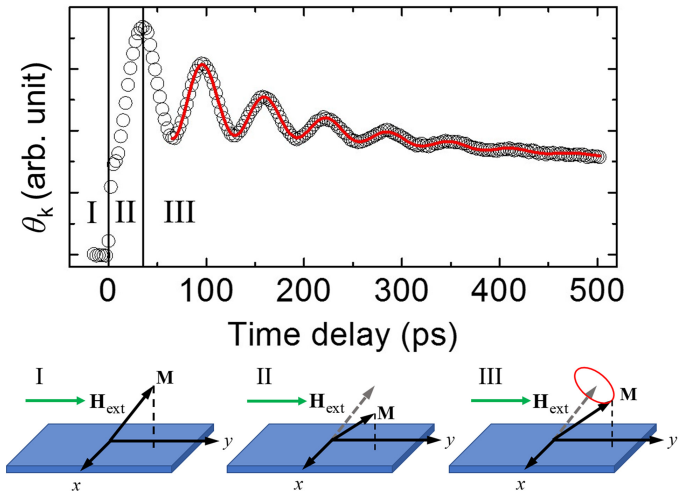

Figure 9.2. The typical signal of magnetic precession from polar TR-MOKE (open symbols). In region I, the system is in equilibrium with the magnetization (**M**) canted by an external field ($\mathbf{H}_{ext}$) to be along $\mathbf{H}_{eff}$. Following the laser pulse heating, both the saturation magnetization and magnetic anisotropy will decrease, which results in a change in the minimum energy direction in region II. After some amount of time, M_s will recover, but the angle between **M** and $\mathbf{H}_{eff}$ will result in precession (region III). The solid line indicates the fit of the data to a decaying sinusoid as expressed by equation (9.13). In regions I and III, $\mathbf{H}_{eff}$ is pointing along the equilibrium direction as denoted by the gray dashed line.

and magnetic anisotropy decrease, resulting in a change in $\mathbf{H}_{eff}$. Next, as the magnetic material cools down, M_s and magnetic anisotropy begin to recover to their initial values, restoring the minimum energy direction back to the original equilibrium direction. At this point, **M** does not align with $\mathbf{H}_{eff}$, resulting in a torque that acts on **M**. This torque causes damped precessional motion around the equilibrium direction, as described by the LLG equation with a damping parameter (α) and the gyromagnetic ratio (γ) [83]:

$$\frac{d\mathbf{M}}{dt} = -\gamma \mathbf{M} \times \mathbf{H}_{eff} + \frac{\alpha}{M_s}\left(\mathbf{M} \times \frac{d\mathbf{M}}{dt}\right). \tag{9.3}$$

After some mathematical manipulation, equation (9.3) will provide the theoretical foundation to analyze TR-MOKE measurement data for extracting both the spin precession frequency (f) and (α), which will be discussed further in section 9.4.

9.2.2 Optical setup of time-resolved magneto-optical Kerr effect

The TR-MOKE metrology belongs to the ultrafast pump–probe technique that uses a femtosecond laser to first pump energy into a material and then to probe the material response. The major difference between the TR-MOKE and TDTR techniques is the type of signals collected by the probe beam. In TR-MOKE measurements, the polarization state of the probe beam reflected from the sample is monitored [84], while in TDTR measurements, the reflectivity from the sample

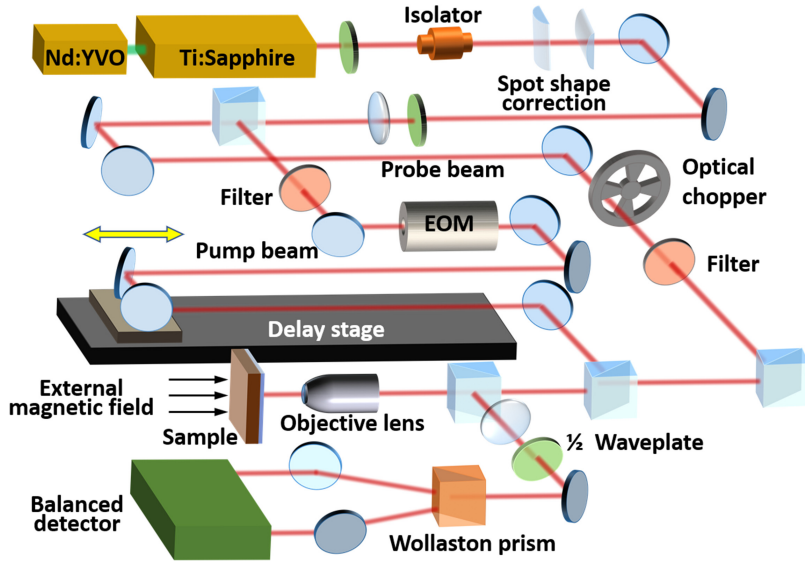

Figure 9.3. A schematic for the TR-MOKE measurement system. Reproduced with permission from [85]. Copyright 2016 the American Chemical Society.

surface is collected. For a small temperature rise, both TR-MOKE and TDTR signals can be treated as linearly proportional to the temperature variation of the sample.

Figure 9.3 depicts the optical layout of an example TR-MOKE set-up at the University of Minnesota, Twin Cities [40], which is upgraded from the basic two-tint time-domain thermoreflectance setup [41]. In TR-MOKE, a mode-locked Ti: Sapphire laser generates a train of pulses (typically ~100 fs in duration) at a repetition rate of 80 MHz (12.5 ns between pulses). An isolator placed right after the laser output prevents the back reflection of light into the laser cavity. The beam shape is corrected by a pair of cylindrical lenses to produce a circular beam spot (preferred for in-plane thermal transport measurements). A polarizing beam splitter separates the laser into pump and probe beams with orthogonal polarizations. The pump beam is modulated with an electro-optical modulator synchronized to a function generator, typically operated at a tunable frequency in the range of 0.1–20 MHz. The probe beam is modulated by a mechanical chopper (~200 Hz). The optical path of the pump beam can be adjusted by a delay stage, which produces a time separation of up to 4 ns between pump heating and probe sensing. The diffraction-limited beam spot size ($1/e^2$ radius) at the sample surface ranges from one to a few tens of micrometers, depending on the magnification of the objective lens [60]. A set of optical filters is exploited to create a spectral separation between pump and probe to suppress pump light that might otherwise leak into the detector. An electromagnet is placed near the sample to provide external magnetic fields (H_{ext}) for the sample.

To facilitate TR-MOKE measurements, a Wollaston prism in conjunction with a balanced detector (photodiode) are used to capture the Kerr rotation angle of the probe beam reflected from the sample. Caution should be exercised to carefully balance the photodiode prior to conducting a measurement, to suppress non-MOKE signals. Additional steps such as differential measurements can also be taken to reduce the non-MOKE components received by an imperfectly balanced detector [63, 66]. The output signal from the balanced detector is sent to a radio-frequency (RF) lock-in amplifier and then to a computer for signal processing with a digital audio-frequency (AF) lock-in. This double-modulation and double lock-in technique allows for the detection of low-level Kerr rotation signals. A more detailed description of the signal analysis for thermal and magnetic transport studies will be discussed, respectively, in sections 9.3 and 9.4.

9.3 Thermal measurements

At a fundamental level, TR-MOKE can be applied for thermal transport studies by correlating the magnetization variation of the material to its temperature excursion. In this section, we derive the relationship between MOKE signals and the temperature of a magnetic material and provide the detailed procedures for the data reduction of thermal measurements. Following that, we present examples of TR-MOKE measurements of several representative materials that are thermally anisotropic. These examples demonstrate the improved measurement sensitivity of TR-MOKE, compared to TDTR, to the in-plane thermal transport within materials.

9.3.1 Temperature information from TR-MOKE signals

Unlike TDTR which uses optically opaque and non-magnetic metallic films as the transducer to absorb light and to probe temperature, TR-MOKE can incorporate magnetic films that are optically semitransparent. When the magnetic transducer is pumped by a laser pulse, it undergoes a process of angular momentum transfer at short time scales, known as ultrafast demagnetization. The thermally induced demagnetization significantly alters the thermodynamic equilibrium among electrons, phonons and magnons and is then followed by a re-magnetization (or recovery) process which happens over times of 1–100 ps [86–91]. The polarization state change of the probe beam reflected from the magnetic transducer, or Kerr rotation change ($\mathrm{d}\theta_\mathrm{k}$), is temperature-dependent. When the temperature rise (ΔT) of the material is small, the signal (S) collected from TR-MOKE measurements is linearly proportional to ΔT:

$$S \approx \frac{\mathrm{d}S}{\mathrm{d}T}\Delta T = \gamma R \frac{\mathrm{d}\theta_\mathrm{k}}{\mathrm{d}T}\Delta T, \tag{9.4}$$

where R is the reflectivity and γ is a conversion coefficient from the optical signal to electrical signal, taking into account the lock-in amplification and gain factors of other electronic devices. The temperature dependence of the Kerr rotation angle, $\mathrm{d}\theta_\mathrm{k}/\mathrm{d}T$, is defined as the thermo-magneto-optical coefficient, which is analogous to

the thermoreflectance coefficient ($\mathrm{d}R/\mathrm{d}T$) in TDTR. Both coefficients represent the responsivity (via either the Kerr rotation angle or the reflectivity) of a transducer to a temperature change. With a first approximation, $\mathrm{d}\theta_\mathrm{k}/\mathrm{d}T$ can be related to the magnetization of the magnetic transducer film:

$$\frac{\mathrm{d}\theta_\mathrm{k}}{\mathrm{d}T} = \frac{\mathrm{d}\theta_\mathrm{k}}{\mathrm{d}M}\frac{\mathrm{d}M}{\mathrm{d}T} = \frac{\mathrm{d}\theta_\mathrm{k}}{\mathrm{d}M/M_\mathrm{s}}\frac{\mathrm{d}M/M_\mathrm{s}}{\mathrm{d}T}. \tag{9.5}$$

Since θ_k is linearly proportional to M and is equal to zero when M equals zero, $\mathrm{d}\theta_\mathrm{k}/\mathrm{d}M$ can then be written as

$$\frac{\mathrm{d}\theta_\mathrm{k}}{\mathrm{d}M} \approx \frac{\theta_\mathrm{ks}}{M_\mathrm{s}}, \tag{9.6}$$

where θ_ks is the Kerr rotation angle at the saturated magnetization (M_s) state at room temperature [74]. By substituting equations (9.5) and (9.6) into equation (9.4), the MOKE signal (S) is linearly proportional to the product of several original factors:

$$S \propto R\theta_\mathrm{ks}\frac{\mathrm{d}M/M_\mathrm{s}}{\mathrm{d}T}\Delta T = p\Delta T. \tag{9.7}$$

The parameters R, θ_ks and $[\mathrm{d}M/M_\mathrm{s}]/\mathrm{d}T$ construct, together, the linear temperature dependence of the TR-MOKE signal. Similar to $\mathrm{d}\theta_\mathrm{K}/\mathrm{d}T$, the product ($p$) of these parameters remains constant for a certain magnetic material, provided that the temperature rise (ΔT) of the material is sufficiently small during TR-MOKE measurements to prevent any nonlinear effects in the $T \sim M$ relation. The product p before ΔT on the right-hand side of equation (9.7) is material dependent and can be optimized for enhancing TR-MOKE signals during thermal measurements. For this purpose, several magnetic materials have been explored as TR-MOKE transducers in the literature, including the 20 nm Co/Pt multilayer studied by Liu *et al* [63] and the 5 nm FePt:Cu ultra-thin alloy films prepared by Kimling *et al* [92]. To systematically investigate and optimize the thermo-magneto-optical coefficient (also the product p), Chen *et al* synthesized magnetic thin films of rare-earth transition metal (RE-TM) alloys and multilayer structures. They demonstrated that among the materials they tested, RE-TM alloys (TbFe) with an optimal thickness of ~20 nm provided the highest signal-to-noise ratio (SNR) for TR-MOKE measurements of thermal properties [85]. They further revealed the origin of TR-MOKE signals and attributed the SNR enhancement to the lower Curie temperatures and larger θ_ks at the laser operating wavelengths of RE-TM alloys. Since TR-MOKE is an emerging technique, there have been limited studies of the material selection and characterization for magnetic transducers. Further efforts should be devoted to identifying magnetic transducers for TR-MOKE thermal measurements under different conditions, such as varied temperature, pressure and laser wavelength.

9.3.2 Measurement process and data analysis of TR-MOKE

Similar to other optical pump–probe methods applied for thermal measurements, in TR-MOKE, the sample is coated by a transducer film (magnetic) with known properties and structural parameters, including thermal conductivity, specific heat and film thickness. These parameters will be used as inputs for the heat diffusion model for data analysis. For the ease of optical alignment and experimental operation, the polar MOKE configuration is preferred, in which the laser beam is normally incident onto to the sample surface. For this polar MOKE configuration, a magnetic transducer with PMA (the magnetization is along the through-plane direction parallel to the film surface normal) can be used to optimize the Kerr rotation signal. In addition, normal incidence in polar MOKE can also produce a circular beam spot shape that is preferred for in-plane thermal measurements. The circular beam shape can simplify the thermal analysis based on the heat diffusion model.

The in-phase (V_{in}) and out-of-phase (V_{out}) signals are collected by the RF lock-in amplifier in TR-MOKE experiments. Prior to the acquisition of each signal, the magnetic transducer is magnetized to saturation with an external magnet. The magnetization orientation of the magnetic layer can be flipped by reversing the polarity of the external magnet. Each sample is measured twice: with the initial magnetization orientation, and its reverse, referred to as $M+$ and $M-$. As shown in figure 9.4(A), both V_{in} and V_{out} change sign when the initial magnetization is flipped from $M+$ to $M-$. The actual signal used for thermal analysis is the corrected signal taken as the difference between the signals of two measurements with opposite magnetization orientations, which excludes contributions from all non-MOKE components (e.g. thermoreflectance signals). By fitting the time-resolved ratio ($-V_{in}/V_{out}$) from TR-MOKE measurements (figure 9.4(B)) to the heat diffusion model (similar to what is done in TDTR), the through-plane thermal transport properties of the sample underlying the magnetic transducer can be extracted [39, 66].

9.3.3 High-sensitivity thermal measurements enabled by TR-MOKE

Higher measurement sensitivity and therefore better measurement precision are always of critical importance for metrology advancement. For thermal transport studies based on the pump–probe technique, the measurement sensitivity to thermal properties of the sample can be strongly influenced by the transducer's properties and structural parameters. Generally speaking, thinner transducers with low thermal conductivities are beneficial for improving the measurement sensitivity to the thermal properties of the underlying sample material. In TDTR, thin films of aluminum (Al) are commonly chosen as metal transducers owing to the large thermoreflectance coefficient of Al at the laser operating wavelength (near-infrared) and strong adhesion between Al and the sample. This transducer film needs to be optically opaque (typically 70–100 nm) such that thermoreflectance signals of the underlying material will not contribute to the transient reflectivity [41]. TR-MOKE can instead work with optically thin magnetic transducers, which are immune to

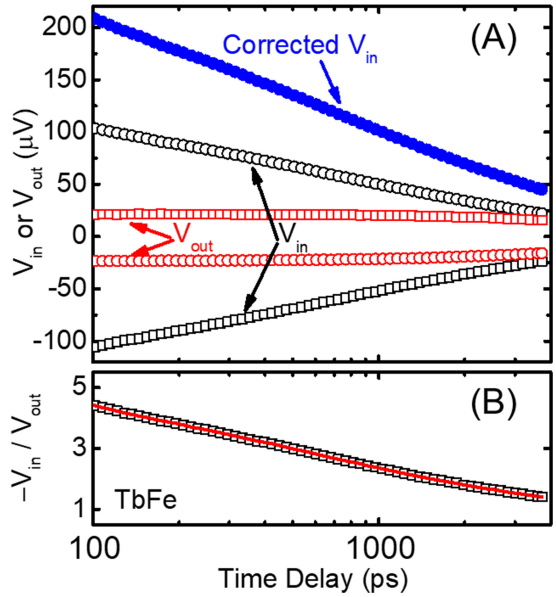

Figure 9.4. Example of the through-plane thermal measurements signal from TR-MOKE on a reference sample of a 300 nm SiO_2 film with an 11.5 nm TbFe transducer layer. (A) In-phase (V_{in}) or out-out-phase (V_{out}) voltage measured via TR-MOKE will change signs depending on the initial magnetization state. Prior to the measurement, the sample is magnetized out-of-plane along either the positive ($M+$) or negative ($M-$) direction resulting in flipped signs for V_{in} and V_{out}. The corrected V_{in} signal is the difference between the V_{in} from $M+$ and $M-$ to exclude non-MOKE signals. (B) The ratio with the corrected V_{in} is fitted to the thermal model to extract the through-plane thermal properties of the sample. Reproduced with permission from [85]. Copyright 2016 the American Chemical Society.

contamination by thermoreflectance signals from the sample itself. For this reason, the thickness of the magnetic transducer can be significantly reduced to enhance the measurement sensitivity to the thermal conductivity of the materials.

For measurements of thermal transport in the through-plane direction, TR-MOKE also provides a better sensitivity to interfacial thermal conductance (G). Using the standard TDTR method, it can be challenging to probe G between dissimilar materials (i.e. materials with large contrasts in stiffness or in the spectra of heat carriers' density of states), such as the interface between metals and oxides (e.g. Al/SiO_2). Using TR-MOKE, Kimling *et al* deposited ultra-thin Co/Pt magnetic layers (4.2–8.2 nm) as magnetic transducers to measure the G values between SiO_2 thin films (with thicknesses of 26–440 nm) and Si substrates [93]. They obtained an unexpected high value of G that is approximately 1.4 GW m^{-2} K^{-1}, which is challenging to detect using TDTR with optically opaque non-magnetic transducers.

As for in-plane thermal measurements, TR-MOKE has even more critical advantages to achieve higher sensitivities, and thus it is well aligned for studying the anisotropic thermal transport properties of 2D materials, such as graphene, h-BN, BP and MoS_2 [35–38]. To measure in-plane thermal transport, TR-MOKE also adopts the 'beam-offset' approach [59, 94]. The full-width at half-maximum

(FWHM) of V_{out} at a negative time delay is recorded as a function of the in-plane offset distance between the pump and probe beams. A heat conduction model taking into account the anisotropy in the materials' transport properties and heat source intensity profiles can be used to extract the sample's thermal conductivity tensor from the measured beam-offset data, given that the beam spot size is comparable to, or smaller than, the in-plane thermal penetration length (related to the heating modulation frequency) [60]. In addition to the small film thickness (<20 nm), the magnetic transducer typically has a lower thermal conductivity (<20 W m^{-1} K^{-1}) resulting from the multilayer or alloy structures. This can suppress the heat spreading in the transducer, and thus the signal contains more information about thermal transport along the in-plane direction within the sample beneath. Therefore, by using optically thin magnetic transducers with low thermal conductivities, TR-MOKE provides reduced systematic errors for measuring in-plane thermal transport [60].

Figure 9.4 summarizes several representative examples of TR-MOKE measurements of in-plane thermal transport from the literature. Zhu *et al* investigated the 3D thermal conductivity of single-crystal BP flakes along the three primary crystalline orientations using TR-MOKE with a 28 nm film of the TbFe alloy as the magnetic transducer [66]. The beam-offset approach was adopted to generate a 2D contour plot of V_{out}, by scanning the pump beam both vertically and horizontally, as shown in figure 9.5(A). The elliptical (instead of circular) shape of the 2D contour plot indicates the anisotropic in-plane thermal transport in BP. A line-cut can be made along any direction (preferably the primary crystalline direction, along the major and minor axes of the ellipse) from the 2D contour to generate the FWHM of V_{out} versus offset distance between pump and probe beams. Therefore, the 2D-scanning beam-offset method does not require a precise sample alignment with a specific crystalline orientation for sample loading, which greatly reduces the difficulties in thermal characterization of anisotropic samples that are a few micrometers in size. For example, in the measurements conducted by Zhu *et al*, the *X*-axis of the beam-offset direction (white solid line) was pre-aligned roughly along the zigzag orientation of the BP flake (the major axis of the ellipse, white dashed line). This 7° difference can be corrected in the data analysis.

Figure 9.5(B) shows the beam-offset signals taken as the line-cut from the 2D contour plot along the two primary crystal orientations indicated by the white dashed lines in figure 9.5(A). The values of the FWHM of measured V_{out} were compared with those predicted from the thermal model to obtain the in-plane thermal conductivity of BP along either the zigzag or armchair direction. The in-plane thermal conductivities of BP fitted from measurement data were 91 ± 10 W m^{-1} K^{-1} along the zigzag direction and 26 ± 3 W m^{-1} K^{-1} along the armchair direction. Rotating the sample by 90° and taking another beam-offset measurement of the same BP flake resolves the same thermal properties of BP, as demonstrated in [66]. The small difference (less than 1% in the FWHM of V_{out}) between the two measurements with different sample loading orientations was within the expected experimental uncertainty, justifying the effectiveness and reliability of this beam-offset TR-MOKE method.

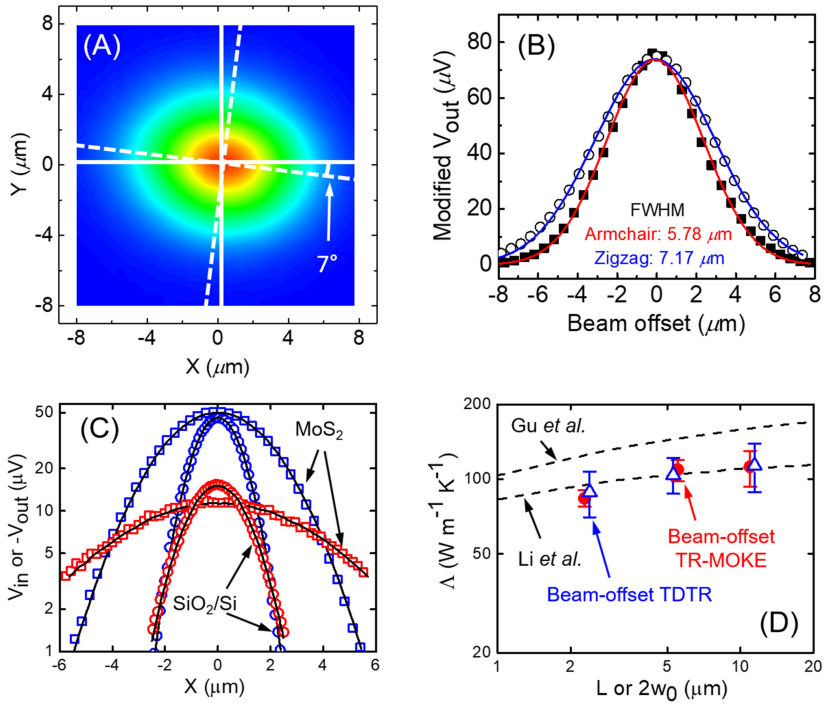

Figure 9.5. In-plane beam-offset TR-MOKE measurement examples. (A) 2D contour measured on a BP flake coated with 28 nm TbFe transducer, taken at a negative time delay ($t = -50$ ps) with a 20× objective lens and 1.6 MHz modulation frequency. The beam-offset signals in (B) are extracted from (a) along the dashed lines denoting the major and minor axes of the ellipse, which correspond to the zigzag and armchair directions, respectively [66]. (C) Beam-offset TR-MOKE data for SiO_2 film (open circles) and MoS_2 (open squares) coated with a 20 nm Co/Pt transducer. V_{out} signals at negative time delay ($t = -100$ ps) with a 20× objective lens and 1 MHz modulation frequency on MoS_2 were used to extract the FWHM [63]. (D) The beam-offset TR-MOKE (red circles) and beam-offset TDTR (blue triangles) measurement results of the MoS_2 in-plane thermal conductivity measured with three different beam spot sizes (w_0). The *ab initio* calculations of thermal conductivity for monolayer MoS_2 by Li *et al* [95] and by Gu and Yang [96] are included for comparison. Figures 9.5(C) and 9.5(D) are adapted from [63] with the permission of AIP Publishing.

The in-plane thermal conductivity of another 2D material, single-crystal MoS_2, was investigated by Liu *et al* [63] using beam-offset TR-MOKE. Their perpendicular magnetic transducer was a Co/Pt multilayer stack with a total thickness of 20 nm. As shown in figure 9.5(C), the beam-offset signals were collected and fitted by Gaussian functions to obtain the FWHM, which was then compared with thermal model predictions, similar to the procedures done for BP. The main difference between these two studies lies in the treatment of the in-plane thermal anisotropy. Liu *et al* did not take a full TR-MOKE 2D contour in [63] since it was assumed that crystalline MoS_2 is thermally isotropic in plane. Figure 9.5(D) shows the in-plane thermal conductivity of the MoS_2 crystal from beam-offset TR-MOKE measurements using three beam spot sizes. For comparison, Liu *et al* also performed beam-offset TDTR measurements of a MoS_2 crystal coated with a 65 nm NbV transducer.

They found that the thermal conductivity data obtained from TR-MOKE and TDTR were consistent, and TR-MOKE provided much smaller error bars. For example, when a 50× objective lens was used with the 20 nm Co/Pt transducer, the uncertainty for TR-MOKE measurements was reduced by nearly a factor of 3, compared to that of TDTR measurements with the 65 nm NbV transducer.

The difference in uncertainty between TDTR and TR-MOKE can be revealed through a sensitivity analysis, which further illustrates how much the TR-MOKE method with a thinner transducer will improve the measurement sensitivity to the in-plane thermal conductivity. For the through-plane thermal conductivity measurements using either TR-MOKE or TDTR, the sensitivity of the ratio signal $(-V_{\text{in}}/V_{\text{out}})$ to a nominal parameter 'σ' is defined as

$$S_z(\sigma) = \frac{\partial[\ln(-V_{\text{in}}/V_{\text{out}})]}{\partial[\ln(\sigma)]}, \tag{9.8}$$

where σ represents one of the geometrical parameters or material's thermal properties and the subscript 'z' denotes the through-plane direction. For in-plane beam-offset measurements, the FWHM of the V_{out} signals at negative time delay is analyzed; thus, the sensitivity of in-plane thermal transport measurements is defined as

$$S_r(\sigma) = \frac{\partial[\ln(\text{FWHM})]}{\partial[\ln(\sigma)]}, \tag{9.9}$$

where the subscript 'r' denotes the in-plane radial direction for general thermal properties.

Figure 9.6 depicts the absolute sensitivity plots of the through-plane TR-MOKE measurements with a 27 nm TbFe transducer, and in-plane beam-offset measurements with both the 27 nm TbFe (used in TR-MOKE) transducer and an 81 nm Al transducer (used in TDTR). The subscript 'm' refers to transducer parameters. The sensitivity analysis of through-plane thermal measurements is calculated for a reference sample of 300 nm SiO_2 on a Si substrate. At long time delay (>100 ps), the heat capacity of the TbFe transducer (C_{m}) is the dominant parameter with the largest measurement sensitivity. Unlike C_{m}, the through-plane measurements are nearly insensitive to the thermal conductivity of the TbFe transducer. This allows the heat capacity of the TbFe transducer to be uniquely determined (figure 9.6(A)). Figure 9.6(B) shows the sensitivities of beam-offset measurements using the same 27 nm TbFe transducer, as a function of the sample in-plane thermal conductivity. The analysis is conducted for the case of a beam spot size of $w_0 = 3$ μm, a laser modulation frequency of $f = 1.6$ MHz, and at a negative time delay of −50 ps. When the Al transducer is used for in-plane TDTR, the large in-plane thermal conductivity of Al ($\Lambda_{r,\text{m}} = 180$ W m^{-1} K^{-1}) causes significant heat spreading in the Al transducer layer, reducing the in-plane measurement sensitivity to Λ_r (figure 9.6(C)). Comparing the sensitivities of TR-MOKE and TDTR depicted in figure 9.6(B) and (C), the sensitivity of TR-MOKE to Λ_r is two to three times higher than that of TDTR, over the entire calculation range. On the other hand, the sensitivity of

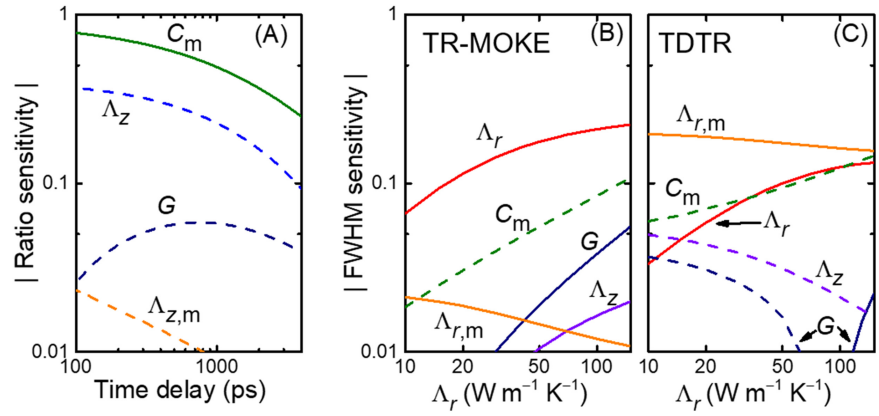

Figure 9.6. Sensitivity analysis of the through-plane and in-plane measurements to different parameters. (A) Absolute ratio sensitivities of through-plane TR-MOKE measurements to the thermal conductivity and heat capacity of a 27 nm TbFe transducer film on 300 nm SiO_2 reference. The measurement conditions are $w_0 = 12$ μm and $f = 9$ MHz. Beam-offset FWHM sensitivities for (B) TR-MOKE with a 27 nm TbFe transducer and (C) TDTR with an 81 nm Al metal transducer as a function of the in-plane thermal conductivity Λ_r measured with $w_0 = 3$ μm and $f = 1.6$ MHz. The time delay is set to -50 ps in both (B) and (C). Solid lines represent the positive values of sensitivities, while dashed lines represent negative sensitivities.

TR-MOKE to $\Lambda_{r,m}$ is one order of magnitude lower than that of TDTR; thus, the use of magnetic transducers in TR-MOKE will also make the measurement results less influenced by the uncertainties of the transducer properties or geometric parameters. Both effects are favored for reducing the overall uncertainty of the in-plane TR-MOKE measurements.

9.4 Ultrafast magnetization dynamics

As pointed out in section 9.1, TR-MOKE is a technique that can be used to study the magnetization dynamics, in addition to thermal transport in materials. In this section, we will focus on detailing the measurement procedures and data analysis for probing the magnetization damping parameters of PMA materials that are of technological importance.

Relating the dynamic magnetization direction to a Kerr rotation (θ_k) requires the consideration of the optical incidence angle. Solving for the Kerr rotation through Fresnel coefficients [70, 71], it can be shown that, for the polar MOKE configuration with normal incidence, θ_k will only contain information from the magnetization component that is along the surface normal (M_z). For oblique incidence, θ_k will contain information from other magnetization components, such as longitudinal MOKE (where **M** is in the plane of incidence and perpendicular to the surface normal), or transverse MOKE (where **M** is perpendicular to both the plane of incidence and the surface normal) [97]. For thermal measurements using TR-MOKE, this distinction between different MOKE metrology is often neglected because the transducer magnetization is saturated along the through-plane direction ($\mathbf{M} = M_z\hat{z}$), and the change in **M** (through temperature variation) can be directly

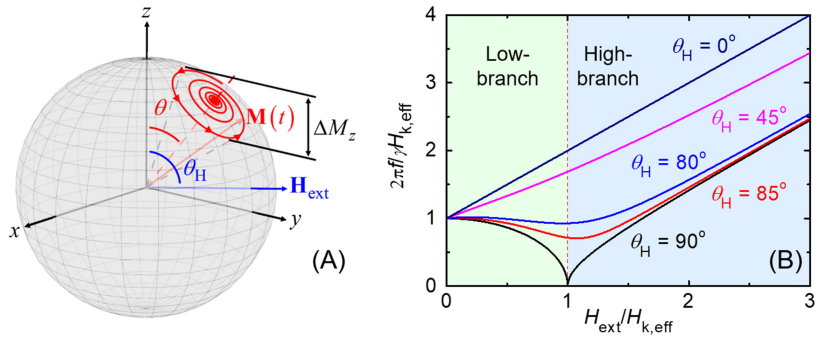

Figure 9.7. Magnetization precession and related key parameters. (A) A 3D representation of the magnetization vector (**M**) precessing around the equilibrium direction (θ) displayed on the surface of a sphere with a radius of M_s. The equilibrium direction is controlled by the magnitude (H_{ext}) and direction (θ_H) of the external magnetic field vector ($\mathbf{H}_{ext}$). The change in the z component of magnetization (ΔM_z) is proportional to the TR-MOKE signal. Reproduced with permission from [117]. Copyright 2018 AIP Publishing. (B) A plot of the resonance frequency (f) normalized to $(\gamma/2\pi)H_{k,eff}$ as a function of H_{ext} normalized to $H_{k,eff}$ for various θ_H. The transition between the low branch ($H_{ext} < H_{k,eff}$) and high branch ($H_{ext} \geqslant H_{k,eff}$) is indicated by different background colors for the $\theta_H = 0°$ case, where the minimum frequency reduces to zero.

related to θ_k without the presence of an external field (H_{ext}). TR-MOKE measurements of magnetization dynamics, on the other hand, utilize an optically induced magnetic torque via thermal demagnetization. Thus, the magnetization response of a material upon optical excitation depends on the direction of the incoming light. While MOKE can be used to determine a 3D profile of the magnetization precession [98], it is often beneficial to reduce the model complexity by focusing on a single component of **M** (such as M_z here).

9.4.1 Magnetization information from TR-MOKE signals

As introduced in section 9.2, the magnetization dynamics in a ferromagnetic film can be described with the LLG equation. Because TR-MOKE operates in the time domain, it is helpful to understand the time-domain response of materials following this differential equation. For this purpose, it is beneficial to transform the LLG equation (equation (9.3)) to a form closer to the original Landau–Lifshitz equation with relaxation [99]:

$$\frac{d\mathbf{M}}{dt} = -\frac{\gamma}{1+\alpha^2}\mathbf{M}\times\mathbf{H}_{eff} - \frac{\gamma}{1+\alpha^2}\frac{\alpha}{M_s}\mathbf{M}\times(\mathbf{M}\times\mathbf{H}_{eff}). \tag{9.10}$$

With this transformation, the use of a spherical coordinate system (as shown in figure 9.7(A)), the assumption that M_s is not changing in time and the small angle approximation, equation (9.10) will result in an eigenvalue problem akin to a damped oscillator system. Solving for the eigenvalue provides a complex resonance frequency (ω) with the real part of this resonance frequency (for $\alpha \ll 1$) described by the Smit–Suhl equation [100, 101]:

$$\omega = \frac{\gamma}{M_s \sin(\theta)} \sqrt{\frac{\partial^2 F}{\partial \theta^2}\frac{\partial^2 F}{\partial \varphi^2} - \left(\frac{\partial^2 F}{\partial \varphi \partial \theta}\right)^2}, \tag{9.11}$$

which relates the angular resonance frequency (ω) to the curvature of magnetic free energy density (F) with respect to the polar angle (θ), the azimuthal angle (φ) and the gyromagnetic ratio (γ). The Smit–Suhl equation is a generalized form of the well-known Kittel dispersion of FMR [20]. The imaginary part of the resonance frequency is the damping rate (inverse of relaxation time, $1/\tau$):

$$\frac{1}{\tau} = \frac{1}{2}\frac{\alpha\gamma}{M_s}\left(\frac{\partial^2 F}{\partial \theta^2} + \frac{1}{\sin^2(\theta)}\frac{\partial^2 F}{\partial \varphi^2}\right). \tag{9.12}$$

The resulting magnetization dynamics can then be represented by a decaying sinusoidal signal, with the frequency being the FMR frequency and the relaxation time which depends on α. For a typical TR-MOKE measurement, the time-dependent signal (S) can be described by

$$S(t) = A + B\exp(-t/C) + D\sin(\omega t + E)\exp(-t/\tau), \tag{9.13}$$

where variables A, B and C relate to the thermal information retained in the measurement (e.g. laser heating induced thermal demagnetization), D is the amplitude of the Kerr rotation resulting from the magnetization precession and E is a phase offset [102]. This measured signal can be treated as proportional to θ_k, given the small temperature rise induced by laser heating during measurements, detector linear responsivity and constant conversion factors of electronic devices. In this way, fitting the TR-MOKE signal to equation (9.13) will result in the FMR frequency and relaxation rate for the measured material. We will next discuss how to relate the measured frequencies and relaxation times to the extraction of important magnetic properties.

9.4.2 Magnetic anisotropy and damping

Magnetic materials with PMA are promising candidates to reduce the switching energy for many technologically important applications [103, 104]. This has led to a large amount of research focused on the magnetic characterization of these materials with TR-MOKE [105–115]. For materials with PMA (and all magnetic systems of interest), we start by defining the magnetic free energy density F, which contains contributions from the Zeeman energy, magnetocrystalline anisotropy (K_u), interfacial anisotropy (K_i) and shape-induced demagnetization energy. The macrospin approximation (treating the material as uniform in space represented by a single-spin mode) for a thin-film material results in

$$F = F_0 - \mathbf{M}\cdot\mathbf{H}_{ext} - K_u(\hat{u}\cdot\mathbf{m})^2 - \left(\frac{K_i}{h} - 2\pi M_s^2\right)(\hat{z}\cdot\mathbf{m})^2, \tag{9.14}$$

where F_0 is the initial free energy density, H_{ext} is the externally applied magnetic field, $\hat{u}$ is the easy axis of the material (low-energy direction), $\mathbf{m}$ is a unit vector along

the direction of the magnetization and h is the thickness of the magnetic film. The term F_0 is independent of magnetization or field and thus does not contribute to dynamics, so is often omitted in the discussions of free energy density. For samples with PMA, F can be expressed in terms of previously defined angles:

$$F = -M_s H_{ext}[\sin(\theta)\sin(\theta_H)\cos(\varphi) + \cos(\theta)\cos(\theta_H)] - K_{eff}\cos^2(\theta), \tag{9.15}$$

where K_{eff} contains the sum of K_u, K_i and the shape (demagnetization) anisotropy, θ_H is the polar angle of the external applied field, and θ and φ correspond to the polar and azimuthal angles of the magnetization, respectively. For magnetic materials with uniaxial perpendicular anisotropy, the azimuthal component of the external field (φ_H) is not considered because the azimuthal angle φ always follows φ_H. The first derivatives of this energy with respect to θ and φ indicate the energy minima, thus providing the equilibrium direction of magnetization:

$$\varphi = 0, \tag{9.16}$$

$$2H_{ext}\sin(\theta_H - \theta) = H_{k,eff}\sin(2\theta), \tag{9.17}$$

where $H_{k,eff}$ is the effective anisotropy field ($H_{k,eff} = 2K_{eff}/M_s - 4\pi M_s$), which indicates the external field required to change the magnetization direction from $\theta = 0°$ to $\theta = 90°$.

Following the Smit–Suhl equation (9.11), the dynamics of the material system can be described by the second derivatives (curvature) of the free energy density F in terms of θ and φ. The resulting equations to describe the resonance frequency (f) are [102]

$$f = \frac{\gamma}{2\pi}\sqrt{H_1 H_2}, \tag{9.18}$$

$$H_1 = H_{ext}\cos(\theta - \theta_H) + H_{k,eff}\cos^2(\theta), \tag{9.19}$$

$$H_2 = H_{ext}\cos(\theta - \theta_H) + H_{k,eff}\cos(2\theta). \tag{9.20}$$

These equations predict the trend of frequency as a function of the external field for a PMA thin film, which is depicted in figure 9.7(B) (the normalized frequency, $f/[(\gamma/2\pi)H_{k,eff}]$, versus normalized field, $H_{ext}/H_{k,eff}$). For the cases of field being aligned close to the in-plane direction, f decreases with increasing H_{ext} (low branch) until H_{ext} surpasses a critical field. After this point, f begins to increase with increasing field (high branch), saturating at a slope of $\gamma/2\pi$. For extreme cases, f increases monotonically with H_{ext} at the slope of $\gamma/2\pi$ when H_{ext} is along the surface normal ($\theta_H = 0°$). When H_{ext} is applied along the in-plane direction ($\theta_H = 90°$), these equations result in a singularity with $f = 0$ at $H_{ext} = H_{k,eff}$, which provides the well-known FMR frequency equations for field applied along the hard axis of a magnetic material [100, 116]:

$$f = \frac{\gamma}{2\pi}\sqrt{H_{k,eff}^2 - H_{ext}^2} \quad \text{for } H_{ext} < H_{k,eff} \text{ (low branch)}, \tag{9.21}$$

$$f = \frac{\gamma}{2\pi}\sqrt{H_{\text{ext}}(H_{\text{ext}} - H_{\text{k,eff}})} \quad \text{for} \quad H_{\text{ext}} \geqslant H_{\text{k,eff}} \text{ (high branch).} \tag{9.22}$$

The measured relaxation time also depends on both θ_{H} and H_{ext}. Based on equation (9.12), the relaxation rate of a PMA thin film is given by

$$\frac{1}{\tau} = \frac{1}{2}\alpha\gamma(H_{\text{l}} + H_2) + \frac{1}{2}\left|\frac{\mathrm{d}\omega}{\mathrm{d}H_{\text{k,eff}}}\right|\Delta H_{\text{k,eff}}, \tag{9.23}$$

where the second term on the right side of equation (9.23) incorporates the inhomogeneous broadening effect (apparent damping resulting from variation in $H_{\text{k,eff}}$ throughout the sample). TR-MOKE results often lump the inhomogeneous broadening (extrinsic) and intrinsic damping contribution into an effective damping [107–109] through the simplified relationship $\alpha_{\text{eff}} = 1/2\pi f\tau$ [109–111, 118]. At sufficiently high fields (relative to $H_{\text{k,eff}}$), the effect of inhomogeneous broadening can be minimized, resulting in $\alpha_{\text{eff}} \approx \alpha$. For several technologically relevant materials with large PMA (such as CoFeB and $L1_0$–FePt), it is challenging to reach high enough fields in experiments. Thus, the determination of α from the measured relaxation time often requires knowledge of the material properties (e.g. $H_{\text{k,eff}}$ derived from frequency measurements), numerical fittings [105, 106, 114] and precisely controlled field angles [115]. Figure 9.8 shows a representative study conducted by Lattery *et al*, exploring the angle and field dependence of the resonance frequency and damping for a PMA CoFeB thin-film sample [106].

Fundamentally, other physical phenomena also contribute to damping, including the scattering of magnons (quantized spin waves) within the material. In particular, two-magnon scattering, an elastic collision causing a uniform precession magnon ($\mathbf{k} = 0$) to scatter into a degenerate magnon ($\mathbf{k} \neq 0$), has been widely studied as an extrinsic form of magnetization damping [119–121]. While a theory exists to predict the magnon dispersion within PMA materials [122], incorporation of this theory into the understanding of TR-MOKE results is still a developing field [112].

With the combination of extrinsic sources of damping, inhomogeneous broadening and thickness dependent damping [123, 124], the measured effective damping in PMA materials can be significantly large [113]. For cases with a large effective damping, it is often necessary to consider the measurement conditions to maximize the precessional signal measured by TR-MOKE for reliable determination of α. Lattery *et al* have shown that, in addition to the frequency and effective damping, the TR-MOKE signal (proportional to ΔM_z) also depends on H_{ext} and θ_{H} [117]. An example is illustrated in figure 9.9(A), in which a contour plot shows the amplitude of TR-MOKE signals as a function of θ_{H} and H_{ext} (normalized to $H_{\text{k,eff}}$). The dashed line in figure 9.9(A) provides guidance on choosing field conditions to maximize the SNR of TR-MOKE measurements for complex samples [117]. Using a macromagnetic simulation, a simpler form of the precessional amplitude can be shown to follow

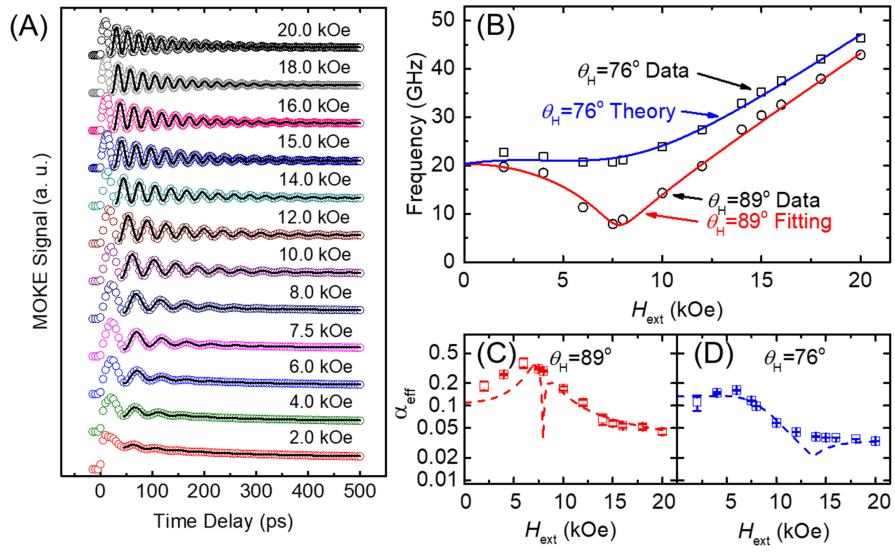

Figure 9.8. The process of data reduction in TR-MOKE measurements of magnetization precession. (A) The raw TR-MOKE signal is fitted to extract f and τ as a function of H_{ext}. (B) The resonance f (calculated from equation (9.18)) is plotted as a function of H_{ext} and fitted to measurement data to extract $H_{k,eff}$ and γ. The circle and square symbols are the measured data with $\theta_H = 89°$ and 76°, respectively. The red line shows the fitting of $\theta_H = 89°$, while the blue line corresponds to the resulting curve generated by using the fitting results from $\theta_H = 89°$ in equation (9.18) for $\theta_H = 76°$. (C) and (D) The inhomogeneous broadening is determined to extract a unique value for α. This α and the inhomogeneous broadening result in a field-dependent α_{eff} (dotted lines), agreeing well with the measured α_{eff} (open squares) for both field angles. Reproduced with permission from [106]. Creative Commons Attribution 4.0 International License.

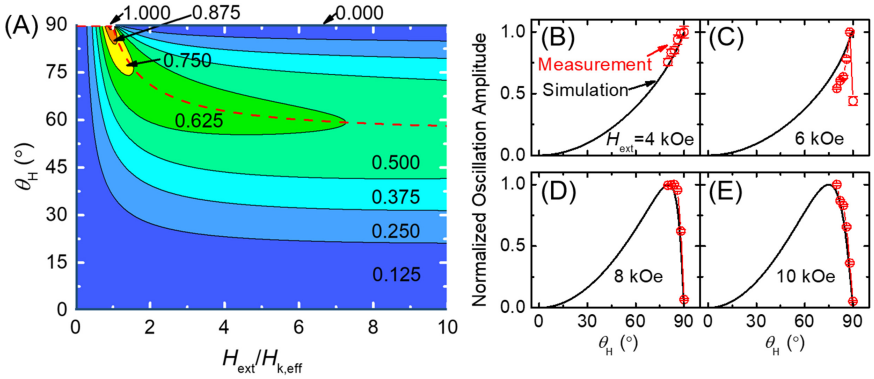

Figure 9.9. Simulation and measurements of TR-MOKE signal optimization for magnetization precession. (A) A contour plot of the normalized ΔM_z signal as a function of the field ratio ($H_{ext}/H_{k,eff}$) and θ_H, where the value of '1' indicates the maximum possible signal. The dotted red line corresponds to $\theta_{H,MAX}$ where the signal is maximized for a specific field ratio. (B)–(E) The measurement results from a W/CoFeB sample (open symbols) compared to a macromagnetic simulation (lines) for various values of H_{ext} normalized to $H_{k,eff}$ (6.1 kOe). Reproduced with permission from [117]. Copyright 2018 AIP Publishing.

$$\frac{\Delta M_z}{M_s} \propto \sin(\theta - \theta_H)\sin(\theta). \tag{9.24}$$

As a demonstration, Lattery *et al* extracted the TR-MOKE signal amplitudes from measurements of a PMA CoFeB thin film seeded with tungsten (W). The results are shown in figure 9.9(B)–(E) as a function of θ_H and H_{ext}. The dependence of TR-MOKE signal amplitudes on these two parameters are in excellent agreement with their model prediction.

This fundamental study of the optimal measurement conditions for higher TR-MOKE SNRs augments the research that has already been conducted with the TR-MOKE metrology for ultrafast magnetization dynamics, showing the versatility of this technique. Building upon an understanding of the FMR, the precession frequency and relaxation in these time-resolved measurements can be processed to extract magnetic properties, including $H_{k,eff}$ and α. As magnetic materials continue to advance, TR-MOKE has already served as a critical tool for understanding the magnetic transport properties and dynamics of these materials and for optimizing their usage and integration into advanced technologies.

9.5 Advanced capabilities for broader research directions

In addition to the studies of thermal properties and Gilbert damping with TR-MOKE, the ultrafast time scale is host to a plethora of physical processes that warrant further research. In this section, we will briefly highlight the potential of extending TR-MOKE capabilities to several other promising research areas.

9.5.1 Propagating spin waves

In analogy to lattice vibrations (phonons), spin waves (magnons) can be treated as oscillations in the magnetization of a material. Because the magnetization in the material is coupled together, when a single spin precesses, it will cause neighboring spins to also move accordingly and thus distribute the precession as waves. These waves lead to a difference in magnetization throughout the sample [125], and thus they can be imaged through interpretation of FMR data [126], or directly through MOKE. These spin waves within ferromagnetic materials are important for the future study of the transfer of spin angular momentum, even in ferrimagnetic insulators [127].

Research in the imaging of spin waves started with the study of standing spin waves in thick metallic films [64]. If the film thickness matches an integer number of magnon half-wavelengths, a standing spin wave will have a resonant frequency that is related to the magnon dispersion (specifically the spin wave exchange stiffness, D) within the material [125, 126]. Recent interests have been focused on studies of ultra-thin ferromagnetic films (less than 10 nm), which do not typically show the standing spin waves [64]. The perturbation from optical excitation can create spin waves that propagate along the in-plane direction of the film [128]. By varying the time delay between the excitation and probe beams (and potentially the distance between them as well), the resulting temporal and spatial map of the magnetization at the sample

surface can detect propagating wave packets of the so-called 'magnetostatic spin waves' [128–130].

9.5.2 Ultrafast energy carrier coupling

As mentioned in section 9.2, due to the ultrafast optical pulses used in TR-MOKE (~100 fs), this technique can capture information about the coupling between energy carriers that is prevalent before the magnetization equilibrates with the electrons and phonons in the system [80]. For non-magnetic materials, the two-temperature model (2TM) has been used to describe the electron–phonon coupling (G_{ep}) [131], but the lack of understanding regarding the transfer and dissipation of angular momentum (and thus magnetization) in magnetic materials requires more complex models to interpret the signals from ultrafast demagnetization processes.

The most often discussed model is the phenomenological three-temperature model (3TM). In 3TM, electrons are heated by the pump pulse and the three thermal reservoirs assigned to lattice (phonons), electron and spin (magnons), respond via inter-reservoir coupling [80]. While useful, 3TM is almost purely phenomenological and reveals limited information about the physical processes that induce demagnetization. Expanding on the concept of this model, other models (such as the microscopic 3TM or M3TM) have incorporated aspects of Elliott–Yafet scattering (magnon–phonon scattering, i.e. a loss of magnon energy to atomic lattice vibrations) to explain the loss of magnetization as a spin-flip scattering event [89, 132]. Although further publications have expanded this model to include spin accumulation and spin currents [133], there have been very few modifications to this model since it was originally proposed.

In parallel with this, there has been an effort to interpret the ultrafast demagnetization through the lens of magnetization dynamics. These models utilize the high-temperature of electrons as an input into atomistic simulations of spin [134]. As such, these models would still require the 2TM and G_{ep} as an input. Where these atomistic spin models differ from the 3TM approach is in the treatment of spin states not as a thermal reservoir, but as individual components of a larger system with their own unique magnetic moments [134]. These temperature-dependent atomistic simulations require a large amount of computational resources to simulate ultrafast magnetization within systems of interest. Therefore, it is often of interest to utilize single-spin (macrospin) approaches, such as the LLB equation, as an approximation [135, 136]. In fact, there are literature studies showing that the LLB approach is approximately equivalent to the M3TM in understanding ultrafast demagnetization processes [137]. As a system-averaged approach to understand high-temperature magnetization, LLB has been argued to fail to consider the change in magnon heat capacity at high temperatures [92], it still offers a useful tool for applications such as HAMR and all-optical switching, where temperature dependence is crucial.

9.5.3 Straintronics (coupling between spin and strain)

Magnetostriction is a well-known phenomenon in which the magnetization within a magnetic material causes a structural deformation and can even launch acoustic strains [138]. The inverse effect is also important, particularly in pump–probe measurements that create longitudinal strain waves via thermal expansion after optical excitation [139, 140]. This strain will create picosecond acoustic signals in TDTR measurements that can be used to determine the thickness of thin films. Through the inverse magnetostriction effect, strain waves can also influence magnetization dynamics, as shown in the study of ferromagnetic Ni films by Kim *et al* [141]. Further research has also shown how this effect can be achieved by using materials with large magnetostriction, such as Galfenol (an alloy of Fe and Ga), [142] or controlling the strain in the material through the use of acoustic Bragg mirrors [143]. Utilizing the coupling between strain and magnetization can potentially offer a unique non-thermal approach to excite magnetization precession for realizing high-speed and low-energy switching in spintronics.

9.5.4 Spin caloritronics

The recent discovery of the spin Seebeck effect [144, 145] has resulted in a large amount of research into the field of spin caloritronics [146, 147]. Analogous to the standard Seebeck effect, the spin Seebeck effect results in a voltage difference when a temperature gradient is present in a magnetic material. While many measurements of the spin Seebeck constant in magnetic materials occur at steady state [144, 145, 148, 149], the ultrafast temperature rise from a pump–probe measurement can lead to the existence of spin currents and spin accumulation (e.g. the accumulation of electron angular momentum at interfaces) at an ultrafast time scale, which can be measured by TR-MOKE [132, 133]. Due to a difference in the density of states of spin up/down electrons in a magnetic material, an ultrafast temperature gradient can also lead to a spin current from the spin-dependent Seebeck effect (not to be confused with the spin Seebeck effect). This spin current then creates a spin-transfer torque that can initiate precession in a ferromagnetic detector layer [132, 150]. These initial measurements have shown the efficacy of measuring spin caloritronics with TR-MOKE, but most of the advances in this field have been determined through other techniques [147].

9.6 Summary and outlook

As technology continues to shrink in scale and technological advancements such as the field of spintronics come to life, it becomes increasingly important to study materials' transport behaviors in the ultrafast time scale. In this chapter, we have discussed a number of applications for TR-MOKE measurements including measurements of thermal properties, magnetization dynamics and the coupling between the two. As we have shown, TR-MOKE has been applied to understand complex materials with high anisotropy and to increase the measurement sensitivity to the thermal transport within materials and across interfaces. The results of these

experimental studies can improve the design of future devices and interfaces for better thermal management. This powerful technique can also measure the dynamic magnetization within ferromagnetic materials, which has already become a crucial demand for spintronic materials and devices. Exciting new research has already utilized TR-MOKE to probe deeper into unique physics such as the coupling between energy carriers, and the phenomena of spin caloritronics.

Acknowledgements

The work described in this chapter was supported by the following funding agencies: the National Science Foundation (NSF) Award No. 1804840, the University of Minnesota MRSEC under the NSF Award No. DMR-1420013, C-SPIN (one of six centers of STARnet, a Semiconductor Research Corporation program, sponsored by MARCO and DARPA), the Legislative-Citizen Commission on Minnesota Resources (LCCMR), the Advanced Storage Research Consortium, 3M, the Institute on the Environment at the University of Minnesota and the Office of the Vice President for Research at the University of Minnesota. DL also appreciates the support from the university's 2019–2020 Doctoral Dissertation Fellowship. Portions of the work related to sample fabrication and characterization were conducted in the Minnesota Nano Center, supported by the NSF through the National Nano Coordinated Infrastructure Network (NNCI) under Award No. ECCS-1542202.

References

[1] Moore G E 2006 *IEEE Solid-State Circuits Soc. Newslett.* **11** 36–7
[2] Theis T N and Wong H P 2017 *Comput. Sci. Eng.* **19** 41–50
[3] Baibich M N, Broto J M, Fert A, Van Dau F N, Petroff F, Etienne P, Creuzet G, Friederich A and Chazelas J 1988 *Phys. Rev. Lett.* **61** 2472–5
[4] Binasch G, Grünberg P, Saurenbach F and Zinn W 1989 *Phys. Rev.* B **39** 4828–30
[5] Tehrani S, Slaughter J M, Chen E, Durlam M, Shi J and DeHerren M 1999 *IEEE Trans. Magn.* **35** 2814–9
[6] Slonczewski J C 1996 *J. Magn. Magn. Mater.* **159** L1–7
[7] Berger L 1996 *Phys. Rev.* B **54** 9353–8
[8] Liu L, Pai C-F, Li Y, Tseng H W, Ralph D C and Buhrman R A 2012 *Science* **336** 555–8
[9] Cubukcu M *et al* 2018 *IEEE Trans. Magn.* **54** 1–4
[10] Behin-Aein B, Datta D, Salahuddin S and Datta S 2010 *Nat. Nanotechnol.* **5** 266
[11] Kim J, Paul A, Crowell P A, Koester S J, Sapatnekar S S, Wang J and Kim C H 2015 *Proc. IEEE* **103** 106–30
[12] Camsari K Y, Faria R, Sutton B M and Datta S 2017 *Phys. Rev.* X **7** 031014
[13] Kiselev S I, Sankey J C, Krivorotov I N, Emley N C, Schoelkopf R J, Buhrman R A and Ralph D C 2003 *Nature* **425** 380
[14] Kaka S, Pufall M R, Rippard W H, Silva T J, Russek S E and Katine J A 2005 *Nature* **437** 389
[15] Houssameddine D *et al* 2007 *Nat. Mater.* **6** 447
[16] Mizushima K, Kudo K and Sato R 2007 *J. Magn. Magn. Mater.* **316** e960–2
[17] Kryder M H, Gage E C, McDaniel T W, Challener W A, Rottmayer R E, Ju G, Hsia Y and Erden M F 2008 *Proc. IEEE* **96** 1810–35

[18] Challener W A *et al* 2009 *Nat. Photonics* **3** 220
[19] Ju G *et al* 2015 *IEEE Trans. Magn.* **51** 1–9
[20] Kittel C 1948 *Phys. Rev.* **73** 155–61
[21] Kittel C 1947 *Phys. Rev.* **71** 270–1
[22] Rossing T D 1963 *J. Appl. Phys.* **34** 995
[23] Farle M, Silva T and Woltersdorf G 2013 *Magnetic Nanostructures: Spin Dynamics and Spin Transport* ed H Zabel and M Farle (Berlin: Springer), pp 37–83
[24] Cahill D G *et al* 2014 *Appl. Phys. Rev.* **1** 011305
[25] Nan C-W, Birringer R, Clarke D R and Gleiter H 1997 *J. Appl. Phys.* **81** 6692–9
[26] Goodson K E and Ju Y S 1999 *Annu. Rev. Mater. Sci.* **29** 261–93
[27] Cahill D G, Bullen A and Seung-Min L 2000 *High Temp. High Press.* **32** 135–42
[28] Soyez G, Eastman J A, Thompson L J, Bai G-R, Baldo P M, McCormick A W, DiMelfi R J, Elmustafa A A, Tambwe M F and Stone D S 2000 *Appl. Phys. Lett.* **77** 1155–7
[29] Hung M-T, Choi O, Ju Y S and Hahn H T 2006 *Appl. Phys. Lett.* **89** 023117
[30] Chiritescu C, Cahill D G, Nguyen N, Johnson D, Bodapati A, Keblinski P and Zschack P 2007 *Science* **315** 351–3
[31] Losego M D, Moh L, Arpin K A, Cahill D G and Braun P V 2010 *Appl. Phys. Lett.* **97** 011908
[32] Gundrum B C, Cahill D G and Averback R S 2005 *Phys. Rev.* B **72** 245426
[33] Hamad-Schifferli K, Schwartz J J, Santos A T, Zhang S and Jacobson J M 2002 *Nature* **415** 152
[34] Vallabhaneni A K, Qiu B, Hu J, Chen Y P, Roy A K and Ruan X 2013 *J. Appl. Phys.* **113** 064311
[35] Novoselov K S, Geim A K, Morozov S V, Jiang D, Katsnelson M I, Grigorieva I V, Dubonos S V and Firsov A A 2005 *Nature* **438** 197
[36] Ferrari A C and Basko D M 2013 *Nat. Nanotechnol.* **8** 235
[37] Rodin A S, Carvalho A and Castro Neto A H 2014 *Phys. Rev. Lett.* **112** 176801
[38] Cai Y, Zhang G and Zhang Y-W 2014 *JACS* **136** 6269–75
[39] Cahill D G 2004 *Rev. Sci. Instrum.* **75** 5119–22
[40] Zhu J, Wu X, Lattery D M, Zheng W and Wang X 2017 *Nanoscale Microscale Thermophys. Eng.* **21** 177–98
[41] Kang K, Koh Y K, Chiritescu C, Zheng X and Cahill D G 2008 *Rev. Sci. Instrum.* **79** 114901
[42] Persson A I, Koh Y K, Cahill D G, Samuelson L and Linke H 2009 *Nano Lett.* **9** 4484–8
[43] Koh Y K, Bae M-H, Cahill D G and Pop E 2011 *ACS Nano* **5** 269–74
[44] Monachon C and Weber L 2012 *Emerg. Mater. Res.* **1** 89–98
[45] Cheaito R, Duda J C, Beechem T E, Hattar K, Ihlefeld J F, Medlin D L, Rodriguez M A, Campion M J, Piekos E S and Hopkins P E 2012 *Phys. Rev. Lett.* **109** 195901
[46] Wang X, Liman C D, Treat N D, Chabinyc M L and Cahill D G 2013 *Phys. Rev.* B **88** 075310
[47] Zhu J, Zhu Y, Wu X, Song H, Zhang Y and Wang X 2016 *Appl. Phys. Lett.* **108** 231903
[48] Zhu J, Feng T, Mills S, Wang P, Wu X, Zhang L, Pantelides S T, Du X and Wang X 2018 *ACS Appl. Mater. Interfaces* **10** 40740–7
[49] Prakash A, Xu P, Wu X, Haugstad G, Wang X and Jalan B 2017 *J. Mater. Chem.* C **5** 5730–6

[50] Liu J, Wang X, Li D, Coates N E, Segalman R A and Cahill D G 2015 *Macromolecules* **48** 585–91
[51] Wang X, Ho V, Segalman R A and Cahill D G 2013 *Macromolecules* **46** 4937–43
[52] Mai C-K, Schlitz R A, Su G M, Spitzer D, Wang X, Fronk S L, Cahill D G, Chabinyc M L and Bazan G C 2014 *JACS* **136** 13478–81
[53] Xu D, Wang Q, Wu X, Zhu J, Zhao H, Xiao B, Wang X, Wang X and Hao Q 2018 *Front. Energy* **12** 127–36
[54] Hopkins P E, Beechem T, Duda J C, Hattar K, Ihlefeld J F, Rodriguez M A and Piekos E S 2011 *Phys. Rev.* B **84** 125408
[55] Losego M D, Grady M E, Sottos N R, Cahill D G and Braun P V 2012 *Nat. Mater.* **11** 502
[56] Hohensee G T, Wilson R B and Cahill D G 2015 *Nat. Commun.* **6** 6578
[57] Zheng K, Sun F, Zhu J, Ma Y, Li X, Tang D, Wang F and Wang X 2016 *ACS Nano* **10** 7792–8
[58] Wu X, Ni Y, Zhu J, Burrows N D, Murphy C J, Dumitrica T and Wang X 2016 *ACS Appl. Mater. Interfaces* **8** 10581–9
[59] Feser J P and Cahill D G 2012 *Rev. Sci. Instrum.* **83** 104901
[60] Feser J P, Liu J and Cahill D G 2014 *Rev. Sci. Instrum.* **85** 104903
[61] Jang H, Ryder C R, Wood J D, Hersam M C and Cahill D G 2017 *Adv. Mater.* **29** 1700650
[62] Jang H, Wood J D, Ryder C R, Hersam M C and Cahill D G 2015 *Adv. Mater.* **27** 8017–22
[63] Liu J, Choi G-M and Cahill D G 2014 *J. Appl. Phys.* **116** 233107
[64] van Kampen M, Jozsa C, Kohlhepp J T, LeClair P, Lagae L, de Jonge W J M and Koopmans B 2002 *Phys. Rev. Lett.* **88** 227201
[65] Barman A, Kimura T, Otani Y, Fukuma Y, Akahane K and Meguro S 2008 *Rev. Sci. Instrum.* **79** 123905
[66] Zhu J *et al* 2016 *Adv. Electron. Mater.* **2** 1600040
[67] Kerr J 1900 *The Effects of a Magnetic Field on Radiation* ed E P Lewis (New York: American Book), pp 27–52
[68] Pedrotti F L, Pedrotti L M and Pedrotti L S 2007 *Introduction to Optics* (London: Pearson Education), p 562
[69] Yang Z J and Scheinfein M R 1993 *J. Appl. Phys.* **74** 6810–23
[70] You C Y and Shin S C 1996 *Appl. Phys. Lett.* **69** 1315–7
[71] You C-Y and Shin S-C 1998 *J. Appl. Phys.* **84** 541–6
[72] Landau L D and Lifshitz E M 1984 *Electrodynamics of Continuous Media* ed L D Landau and E M Lifshitz (Amsterdam: Pergamon), pp 257–89
[73] Krinchik G S and Arem'ev V A 1968 *Sov. Phys. JETP* **26** 1080–5
[74] Qiu Z Q and Bader S D 2000 *Rev. Sci. Instrum.* **71** 1243–55
[75] Huang B *et al* 2017 *Nature* **546** 270
[76] Schmidt F, Rave W and Hubert A 1985 *IEEE Trans. Magn.* **21** 1596–8
[77] Rave W, Schäfer R and Hubert A 1987 *J. Magn. Magn. Mater.* **65** 7–14
[78] Agranat M B, Ashitkov S I, Granovskii A B and Rukman G I 1984 *Sov. Phys. JETP* **59** 804–6
[79] Vaterlaus A, Beutler T, Guarisco D, Lutz M and Meier F 1992 *Phys. Rev.* B **46** 5280–6
[80] Beaurepaire E, Merle J C, Daunois A and Bigot J Y 1996 *Phys. Rev. Lett.* **76** 4250–3
[81] Ju G, Nurmikko A V, Farrow R F C, Marks R F, Carey M J and Gurney B A 1999 *Phys. Rev. Lett.* **82** 3705–8

[82] Ju G, Chen L, Nurmikko A V, Farrow R F C, Marks R F, Carey M J and Gurney B A 2000 *Phys. Rev.* B **62** 1171–7
[83] Gilbert T L 2004 *IEEE Trans. Magn.* **40** 3443–9
[84] Koopmans B 2003 *Spin Dynamics in Confined Magnetic Structures II* ed B Hillebrands and K Ounadjela (Berlin: Springer), pp 253–316
[85] Chen J-Y, Zhu J, Zhang D, Lattery D M, Li M, Wang J-P and Wang X 2016 *J. Phys. Chem. Lett.* **7** 2328–32
[86] Güdde J, Conrad U, Jähnke V, Hohlfeld J and Matthias E 1999 *Phys. Rev.* B **59** R6608–11
[87] Melnikov A, Bovensiepen U, Radu I, Krupin O, Starke K, Matthias E and Wolf M 2004 *J. Magn. Magn. Mater.* **272–276** 1001–2
[88] Wietstruk M, Melnikov A, Stamm C, Kachel T, Pontius N, Sultan M, Gahl C, Weinelt M, Dürr H A and Bovensiepen U 2011 *Phys. Rev. Lett.* **106** 127401
[89] Koopmans B, Malinowski G, Dalla Longa F, Steiauf D, Fähnle M, Roth T, Cinchetti M and Aeschlimann M 2010 *Nat. Mater.* **9** 259–65
[90] Roth T, Schellekens A J, Alebrand S, Schmitt O, Steil D, Koopmans B, Cinchetti M and Aeschlimann M 2012 *Phys. Rev.* X **2** 021006
[91] Hohensee G T, Wilson R B, Feser J P and Cahill D G 2014 *Phys. Rev.* B **89** 024422
[92] Kimling J, Kimling J, Wilson R B, Hebler B, Albrecht M and Cahill D G 2014 *Phys. Rev.* B **90** 224408
[93] Kimling J, Philippi-Kobs A, Jacobsohn J, Oepen H P and Cahill D G 2017 *Phys. Rev.* B **95** 184305
[94] Wang X J, Mori T, Kuzmych-Ianchuk I, Michiue Y, Yubuta K, Shishido T, Grin Y, Okada S and Cahill D G 2014 *APL Mater.* **2** 046113
[95] Li W, Carrete J and Mingo N 2013 *Appl. Phys. Lett.* **103** 253103
[96] Gu X and Yang R 2014 *Appl. Phys. Lett.* **105** 131903
[97] Mansuripur M 1995 *The Physical Principles of Magneto-optical Recording* (Cambridge: Cambridge University Press), pp 128–79
[98] Acremann Y, Back C H, Buess M, Portmann O, Vaterlaus A, Pescia D and Melchior H 2000 *Science* **290** 492–5
[99] Iida S 1963 *J. Phys. Chem. Solids* **24** 625–30
[100] Smit J and Beljers H G 1955 *Philips Res. Rep.* **10** 113–30
[101] Suhl H 1955 *Phys. Rev.* **97** 555–7
[102] Mizukami S 2015 *J. Magn. Soc. Jpn.* **39** 1–7
[103] Mangin S, Ravelosona D, Katine J A, Carey M J, Terris B D and Fullerton E E 2006 *Nat. Mater.* **5** 210
[104] Meng H and Wang J-P 2006 *Appl. Phys. Lett.* **88** 172506
[105] Iihama S, Mizukami S, Naganuma H, Oogane M, Ando Y and Miyazaki T 2014 *Phys. Rev.* B **89** 174416
[106] Lattery D M, Zhang D, Zhu J, Hang X, Wang J-P and Wang X 2018 *Sci. Rep.* **8** 13395
[107] Zhang B *et al* 2017 *Appl. Phys. Lett.* **110** 012405
[108] Song H-S, Lee K-D, Sohn J-W, Yang S-H, Parkin S S P, You C-Y and Shin S-C 2013 *Appl. Phys. Lett.* **103** 022406
[109] Mizukami S, Watanabe D, Kubota T, Zhang X, Naganuma H, Oogane M, Ando Y and Miyazaki T 2010 *Appl. Phys. Exp.* **3** 123001
[110] Iihama S, Sakuma A, Naganuma H, Oogane M, Miyazaki T, Mizukami S and Ando Y 2014 *Appl. Phys. Lett.* **105** 142403

[111] Wu D, Li W, Tang M, Zhang Z, Lou S and Jin Q Y 2016 *J. Magn. Magn. Mater.* **409** 143–7
[112] Iihama S, Sakuma A, Naganuma H, Oogane M, Mizukami S and Ando Y 2016 *Phys. Rev.* B **94** 174425
[113] Becker J, Mosendz O, Weller D, Kirilyuk A, Maan J C, Christianen P C M, Rasing T and Kimel A 2014 *Appl. Phys. Lett.* **104** 152412
[114] Takahashi Y K *et al* 2017 *Appl. Phys. Lett.* **110** 252409
[115] Capua A, Yang S-h, Phung T and Parkin S S P 2015 *Phys. Rev.* B **92** 224402
[116] Morrish A H 1965 *The Physical Principles of Magnetism* (New York: Wiley), p 555
[117] Lattery D M, Zhu J, Zhang D, Wang J-P, Crowell P A and Wang X 2018 *Appl. Phys. Lett.* **113** 162405
[118] Qiao S, Nie S, Zhao J, Huo Y, Wu Y and Zhang X 2013 *Appl. Phys. Lett.* **103** 152402
[119] Sparks M 1964 *Ferromagnetic-Relaxation Theory* (New York: McGraw-Hill)
[120] McMichael R D and Krivosik P 2004 *IEEE Trans. Magn.* **40** 2–11
[121] Landeros P, Arias R E and Mills D L 2008 *Phys. Rev.* B **77** 214405
[122] Beaujour J M, Ravelosona D, Tudosa I, Fullerton E E and Kent A D 2009 *Phys. Rev.* B **80** 180415
[123] Tserkovnyak Y, Brataas A and Bauer G E W 2002 *Phys. Rev. Lett.* **88** 117601
[124] Ikeda S, Miura K, Yamamoto H, Mizunuma K, Gan H D, Endo M, Kanai S, Hayakawa J, Matsukura F and Ohno H 2010 *Nat. Mater.* **9** 721
[125] Kittel C 1958 *Phys. Rev.* **110** 1295–7
[126] Weber R 1968 *IEEE Trans. Magn.* **4** 28–31
[127] Kajiwara Y *et al* 2010 *Nature* **464** 262
[128] Iihama S, Sasaki Y, Sugihara A, Kamimaki A, Ando Y and Mizukami S 2016 *Phys. Rev.* B **94** 020401
[129] Yun S-J, Cho C-G and Choe S-B 2015 *Appl. Phys. Exp.* **8** 063009
[130] Wessels P, Vogel A, Tödt J-N, Wieland M, Meier G and Drescher M 2016 *Sci. Rep.* **6** 22117
[131] Qiu T Q, Juhasz T, Suarez C, Bron W E and Tien C L 1994 *Int. J. Heat Mass Transfer* **37** 2799–808
[132] Choi G-M, Min B-C, Lee K-J and Cahill D G 2014 *Nat. Commun.* **5** 4334
[133] Kimling J and Cahill D G 2017 *Phys. Rev.* B **95** 014402
[134] Kazantseva N, Nowak U, Chantrell R W, Hohlfeld J and Rebei A 2008 *Europhys. Lett.* **81** 27004
[135] Chubykalo-Fesenko O, Nowak U, Chantrell R W and Garanin D 2006 *Phys. Rev.* B **74** 094436
[136] Kazantseva N, Hinzke D, Nowak U, Chantrell R W, Atxitia U and Chubykalo-Fesenko O 2008 *Phys. Rev.* B **77** 184428
[137] Atxitia U and Chubykalo-Fesenko O 2011 *Phys. Rev.* B **84** 144414
[138] Joule J 1842 *Ann. Electr. Magn. Chem* **8** 219–24
[139] O'Hara K E, Hu X and Cahill D G 2001 *J. Appl. Phys.* **90** 4852–8
[140] Hohensee G T, Hsieh W-P, Losego M D and Cahill D G 2012 *Rev. Sci. Instrum.* **83** 114902
[141] Kim J-W, Vomir M and Bigot J-Y 2012 *Phys. Rev. Lett.* **109** 166601
[142] Jäger J V *et al* 2013 *Appl. Phys. Lett.* **103** 032409
[143] Jäger J V, Scherbakov A V, Glavin B A, Salasyuk A S, Campion R P, Rushforth A W, Yakovlev D R, Akimov A V and Bayer M 2015 *Phys. Rev.* B **92** 020404

[144] Uchida K, Takahashi S, Harii K, Ieda J, Koshibae W, Ando K, Maekawa S and Saitoh E 2008 *Nature* **455** 778
[145] Uchida K *et al* 2010 *Nat. Mater.* **9** 894
[146] Bauer G E W, Saitoh E and van Wees B J 2012 *Nat. Mater.* **11** 391
[147] Boona S R, Myers R C and Heremans J P 2014 *Energy Env. Sci.* **7** 885–910
[148] Jaworski C M, Yang J, Mack S, Awschalom D D, Heremans J P and Myers R C 2010 *Nat. Mater.* **9** 898
[149] Jaworski C M, Yang J, Mack S, Awschalom D D, Myers R C and Heremans J P 2011 *Phys. Rev. Lett.* **106** 186601
[150] Choi G-M, Moon C-H, Min B-C, Lee K-J and Cahill D G 2015 *Nat. Phys.* **11** 576